



Image analysis of soft-tissue in-growth and attachment into highly porous alumina ceramic foam metals

A. Khalil^{a,b,*}, C. Aponte^c, R. Zhang^c, T. Davisson^c, I. Dickey^d, D. Engelman^e, M. Hawkins^c, M. Mason^{b,f}

^a Department of Mathematics and Statistics, University of Maine, Orono, ME, United States

^b Institute for Molecular Biophysics, University of Maine/The Jackson Laboratory, Bar Harbor, ME, United States

^c OrthoBiologics, R&D, Stryker Orthopaedics, Mahwah, NJ, United States

^d Adult Reconstruction, Orthopaedic Oncology, Eastern Maine Medical Center, Bangor, ME, United States

^e Department of Molecular Biophysics and Biochemistry, Yale University, New Haven, CT, United States

^f Department of Chemical and Biological Engineering, University of Maine, Orono, ME, United States

ARTICLE INFO

Article history:

Received 13 June 2008

Received in revised form 13 February 2009

Accepted 16 February 2009

Keywords:

Image processing
Fourier analysis
Wavelet Transform
WTMM
Foam metal
Trabecular metal
Artificial bone
Orthopaedics
Implants
Histology

ABSTRACT

The detailed quantitative characterization of soft-tissue in-growth into highly porous artificial implants is critical to understanding the biophysical processes that will lead to the best structural scaffolding construct. Previous studies have performed mechanical peel tests and mostly qualitative histological analyses of soft-tissue. The goal of this paper is to report the results obtained from applying two image analysis algorithms to quantify the morphological structure found in histological images of stained soft-tissue in-growth into alumina ceramic foam metal implants using a canine model. Three different pore sizes were used and three different post-operative time points were considered. Using the 2D Wavelet Transform Modulus Maxima method and 2D Fourier Transform analysis, a strong anisotropic signature (directional preference) is detected in early (4-week) histological samples. The direction of preference is towards the center of the implants. The strength of the anisotropy at later time points (8 and 16 weeks) becomes gradually weaker. Our interpretation is that after a short period of time, the main tissue growth activity has been concentrated on filling the artificial implant by growing towards its center. The weaker anisotropic signature found at later time points is interpreted as the tissue growth activity strengthening its structure by growing in more random directions.

© 2009 IPPEM. Published by Elsevier Ltd. All rights reserved.

1. Introduction

1.1. Alumina ceramic foam

Highly porous foam metals are a family of materials that are constructed out of elements such as titanium, tantalum and nickel. While they are created using various processes, they share a common morphology with a strut/cell like lattice network that is highly interconnected and resembles trabecular skeletal bone, under both gross and microscopic inspection. While this genre of material was initially developed for industrial applications, its subsequent use in biomedical applications, particularly in orthopaedic surgery has revealed extraordinary properties with respect to bone and soft-tissue in-growth abilities. Initial investigation and further work demonstrated that these materials facilitate rapid in-growth of bone and soft-tissue [1,2]. Further investigation demonstrated that

these materials facilitate rapid and well-vascularized in-growth in a wide range of tissue types, including muscle, fascia and subcutaneous tissue, regardless of material type and pore size [3]. Follow-up work with these materials found that they confer true biological function as well, demonstrated by biologic reconstitution of tendon attachment in an established canine model [4–6] with the reconstructed tendon construct exceeding the strength of the non-operative side by 40% at 12 weeks post-operative [7]. Prior to this body of research, all attempts at pure soft-tissue attachment to non-porous metal substrates had been unsuccessful. The implications and importance of these findings bear great relevance for orthopaedic surgical reconstruction in primary and revision joint replacement, sports medicine and oncology surgery where implant longevity, stability, function and patient satisfaction are dependent on stable and functional soft-tissue attachment to the implant construct. The high porosity and degree of interconnectivity of these materials is thought to confer this biological activity, but the specific mechanisms remain unclear and the patterning of the tissue's extracellular matrix inside the pores is not yet understood. Investigation to better understand this process has significant implications in the goals of advancing the development of surgical reconstruction. The crucial starting point is first accurately visualizing and

* Corresponding author at: Department of Mathematics and Statistics, University of Maine, Orono, ME 04469, United States. Tel.: +1 207 581 3911; fax: +1 207 581 3902.

E-mail address: khalil@math.umaine.edu (A. Khalil).

objectively quantifying the bio-response to these foam metals to define what the stages of response and in-growth of this promising metal/tissue interaction are. The next objective is then to assess how alterations in foam metal morphology, such as pore size, shape and volume, affect these growth stages, and ideally, how the expression of growth factors may be modulated. Ultimately, the ability to harness and understand this process could lead to the use of foam metals as effective new scaffolds for tissue engineering and reconstructive surgery.

1.2. Characterizing anisotropy

Signal processing techniques like the two-dimensional (2D) Fourier Transform (FT) and the Wavelet Transform Modulus Maxima (WTMM) methods described here can be used to quantify the roughness of a surface. A rough surface having an anisotropic signature means that the roughness (or pixel intensity variation) of the surface will differ according to the direction considered. Fourier's methods have been used for the analysis of periodic signals in a wide range of disciplines and are now considered fundamental tools in mathematics and the physical sciences [8]. Two-dimensional FT methods have involved the conversion of the Cartesian image into polar coordinates to quantify the anisotropy present in images [9]. Unfortunately, FT methods become very limited when dealing with surfaces having non-homogeneous roughness (*i.e.*, where the image intensity variations are defined locally and not globally). This class of images are referred to as multifractal images. In contrast to the FT, the 2D WTMM method is a multifractal image analysis formalism [10–13], where the different dilations of the analyzing wavelet reveal quantitative roughness information at every size scale considered. The 2D WTMM method has successfully been used in geology for the study of Earth clouds [14], in mammogram radiology to objectively characterize breast tissue types and to discriminate between benign vs. malignant microcalcification clusters in human breast tissue [15,16], in astrophysics for the study of the interstellar medium [13], and in cell biology for the characterization of chromosome territories [17,18]. The superiority of the WTMM method over the FT as well as signal processing techniques like the structure function approach, correlation function, and several others, has been clearly established in previous publications ([10] and references therein). However, in cases where the roughness is homogeneous (as is the case in this paper), both methods are expected to yield similar results [13,19].

1.3. Quantitative histological analysis

Recent studies have used mechanical peel tests to quantify soft-tissue attachment to porous metal in order to find a potential correlation between attachment strength and pore size or between strength and post-operative time [2,3]. Although such correlations are likely to exist, the relatively small sample sizes used in these studies preclude their ability to infer statistically robust conclu-

sions. In order to complement and augment the mechanical tests, histological analyses were also used, but were mainly supported by qualitative and/or visual assessments. The goal of this paper is therefore to present a precise, objective, and rigorously well-defined signal processing approach and to use it to quantify 2D histological images of stained soft-tissue in-growth into porous metal implants by considering the evolution of the anisotropic structure as a function of pore size and post-operative time. The use of both the WTMM and FT methods, combined with the large number of images used for this study allows us to obtain very highly significant statistical results (>99.99% confidence level). Both methods were first calibrated on synthetic isotropic and anisotropic images and then applied to histology images of soft-tissue in-growth into porous artificial implants. For simplicity and ease of comparison, a new quantity called the *anisotropy factor* is introduced. It is important to note that the consideration of the FT results is dependent upon verification of homogeneity of the roughness via the WTMM method. The use of both approaches on several thousand images ensures a very robust statistical analysis and, as both methods concur, demonstrates that our findings are not technique-dependent.

2. Methods

2.1. Implants

Porous alumina rectangular implants were fabricated using reticulated foam technology. The implants were created in three pore sizes: small pore (average pore size of 100–175 μm), medium pore (250–400 μm) and large pore (600–800 μm). Each implant had a final size of 30 mm long, 20 mm wide, and 6 mm thick with a 2-mm diameter hole drilled at each corner to allow the passage of a suture for securing the implant at the time of surgery (Fig. 1A). The implants were processed, cleaned, passivated, packaged and sterilized prior to implantation. The implants were used in an *in vivo* canine model to evaluate soft-tissue in-growth based in part on a protocol published previously [2].

2.2. Animal care

Twelve skeletally mature adult canines weighing approximately 25 kg were used in this study. All study animals were obtained, housed, treated and studied under full institutional I.A.C.U.C. approval at the Mayo Clinic Animal Care Facility. Upon arrival, all animals were subjected to a physical examination by a qualified member of the veterinary staff to ensure a normal health status. The animals were screened to exclude acute and chronic medical conditions during a 3–4 week quarantine period and were housed in standard canine cages throughout the duration of the study. The animal room environment (temperature, humidity, hours of light and dark, and air changes) was monitored and recorded as per AAALAC Standards (a minimum of once every 24 h). Municipal tap

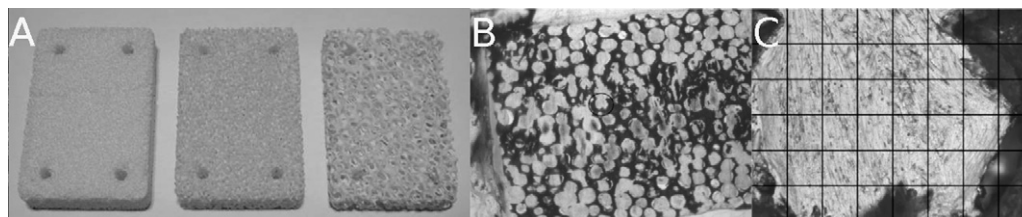


Fig. 1. (A) Alumina ceramic implants showing the small, medium, and large pore samples. Each implant is 30 mm \times 20 mm \times 6 mm in size with a 2 mm diameter hole drilled in each corner for suture fixation. (B) 10 \times zoom of a prepared small-sized pore sample. (C) 200 \times zoom of the circled region shown in (B). The black gridlines in (C) are equally spaced at 256 pixels (\sim 54 μm), showing the lattice used to cut-up the 35 overlapping 512 \times 512 sub-images.

water was provided *ad libitum* (via automatic watering system). A standard certified commercial dog chow was fed to each animal. The animals were groomed, socialized and walked 5 times per week.

2.3. Surgical implantation

The animals were induced by using a combination of Ketamine (10 mg/kg) and Diazepam (0.5 mg/kg) intravenously and maintained by isoflurane inhalation through an anesthetic machine. Standard vital monitoring was utilized intraoperatively for all animals. Surgery was performed using standard aseptic techniques. After the skin was shaved, it was scrubbed with chlorhexidine soap and then swabbed with 70% alcohol. After appropriate anesthesia, each subject had a superficial posterior approach to the spine performed. On each side of the spine, three small subcutaneous pockets via two skin incisions were created between the skin and subcutaneous layer with sharp dissection. One of each pore type block (3 total on each side or 6 total for each animal) was secured with vicryl suture. The wounds were irrigated and then closed in a standard fashion with buried absorbable suture. The animals received standard post-operative care and were given post-operative antibiotics and analgesia (buprenorphine 0.01–0.02 mg/kg q6 h). All animals tolerated the procedure without complication and recovered fully and were post-operatively monitored for signs of infection. Four canines developed a seroma at the surgical site. These seromas were aspective and resolved in three animals. One animal at the time of sacrifice had a remaining seroma of moderate size that was not continuous with the implants and had no sign of infection. The animals were returned to their cages and were ambulatory within 2–3 h. No physical restriction was used. All animals were examined daily by the veterinary staff or staff of the central animal facilities. The animal health technologist associated with the project also checked the dogs weekly.

2.4. Imaging

After harvesting, the specimens were stored in 10% buffered formalin. A 5 mm × 10 mm block was obtained 5 mm from the edge of the block using an Exakt band saw. The samples were dehydrated in graduated alcohol, and were infiltrated and embedded in Technovit 7200. The section was ground to 50–100 μm thick using different grits of paper (from 350 to 1000). One section was cut from each block. Slides were stained with Toluidine Blue or Hematoxylin and Eosin (H&E). The histological slides were observed with a Nikon transmitted light microscope, Microphot-FXA (Nikon, Japan). Digital images were taken with a digital camera coupled to the microscope, MicroPublisher (Qimage, Burnaby BC, Canada) which has a CCD sensor of 3.3 megapixel. The lens on the microscope is 20× lens (Plan 20, Nikon, Japan). The images were pre-processed with Image-Pro Plus software (Media Cybernetics, Inc., Silver Spring, MD). For each sample, 10 different pores were imaged at 200× magnification with a pixel size of ~0.21 μm. In order to provide adequate statistics 26 groups of images were obtained: Three samples were considered for each of the three pore sizes and each of the three time points (3³ = 27), but one of the small pore size samples at 4 week post-operative had to be rejected, yielding the 26 groups. Each of these 26 × 10 = 260 images were digitally segmented into 35 overlapping 512 × 512 sub-images (Fig. 1B and C), resulting in a total starting sample size of N = 9100 images for each time point. Averaging the results over 35 sub-images instead of analyzing the larger original images greatly minimizes edge-effects [10–14], allows to keep only the 512 × 512 sub-images that contain stained soft-tissue and no pore material, and since many samples had been “scratched” during the histological manipulation, the smaller and more abundant sub-images allow for rejection of some of those corresponding sub-images. The rejection of sub-images

based on their content (implant or scratch) was done manually, by visual inspection.

2.5. The 2D Wavelet Transform Modulus Maxima method

The 2D WTMM method is primarily a multifractal analysis tool that provides a way to estimate the fractal dimension of the set of points in the 2D surface that are characterized by a specific local roughness (Hölder) exponent, or in the case of a mono-fractal signature, by a global (Hurst) exponent [10–13]. An anisotropic signature can also be easily detected from the directional information provided by the continuous 2D Wavelet Transform. Let us consider two wavelets that are, respectively, the partial derivatives with respect to *x* and *y* of a 2D smoothing (Gaussian) function. Let

$$\phi_{Gau} = e^{-(x^2+y^2)/2} = e^{-|\mathbf{x}|^2/2} \tag{1}$$

be the Gaussian function, where $|\mathbf{x}| = \sqrt{x^2 + y^2}$, so that

$$\psi_1(x, y) = \frac{\partial\phi_{Gau}(x, y)}{\partial x} \text{ and } \psi_2(x, y) = \frac{\partial\phi_{Gau}(x, y)}{\partial y}. \tag{2}$$

For any 2D function *f*, i.e., an image, the continuous Wavelet Transform of *f* with respect to ψ_1 and ψ_2 has two components and therefore can be expressed in a vectorial form [10,11,13]:

$$\begin{aligned} \mathbf{T}_\psi[f](\mathbf{b}, a) &= (T_{\psi_1}[f], T_{\psi_2}[f]) = \nabla\{\mathbf{T}_{\phi_{Gau}}[f](\mathbf{b}, a)\} \\ &= \nabla\{\phi_{Gau, \mathbf{b}, a} * f\}, \end{aligned} \tag{3}$$

where * represents convolution, and where;

$$\begin{aligned} T_{\psi_1}[f] &= \frac{1}{a^2} \int d^2\mathbf{x} \psi_1\left(\frac{\mathbf{x}-\mathbf{b}}{a}\right) f(\mathbf{x}) \text{ and } T_{\psi_2}[f] \\ &= \frac{1}{a^2} \int d^2\mathbf{x} \psi_2\left(\frac{\mathbf{x}-\mathbf{b}}{a}\right) f(\mathbf{x}) \end{aligned} \tag{4}$$

Here **b** and *a* represent parameters of position and scale respectively. The WT is therefore the gradient vector of *f*(**x**) smoothed by dilated versions of the Gaussian filter, $\phi_{Gau}(\mathbf{x}/a)$. The WT can be written in polar coordinates, i.e., in terms of its modulus and argument:

$$\mathbf{T}_\psi[f](\mathbf{b}, a) = (\mathbf{M}_\psi[f](\mathbf{b}, a), \mathbf{A}_\psi[f](\mathbf{b}, a)) \tag{5}$$

where

$$\begin{aligned} \mathbf{M}_\psi[f](\mathbf{b}, a) &= \sqrt{(T_{\psi_1}[f])^2 + T_{\psi_2}[f]^2} \text{ and } \mathbf{A}_\psi[f](\mathbf{b}, a) \\ &= \mathbf{Arg}(T_{\psi_1}[f] + iT_{\psi_2}[f]). \end{aligned} \tag{6}$$

A very efficient way to perform point-wise regularity analysis is to use the Wavelet Transform Modulus Maxima (WTMM) [20,21]. At a given size scale *a* > 0, the WTMM are defined by the positions **b** where the Wavelet Transform Modulus $\mathbf{M}_\psi[f](\mathbf{b}, a)$ (Eq. (6)) is locally maximum in the direction $\mathbf{A}_\psi[f](\mathbf{b}, a)$ (Eq. (6)) of the gradient vector $\mathbf{T}_\psi[f]$ (Eq. (5)). When analyzing rough surfaces, these WTMM lie on connected chains henceforth called *maxima chains* [10] and are shown as black edge detection lines in Fig. 2B–D. Actually, one only needs to record the position of the local maxima of \mathbf{M}_ψ along the maxima chains together with the values of $\mathbf{M}_\psi[f]$ and $\mathbf{A}_\psi[f]$ at the corresponding locations. At each scale *a*, the wavelet analysis thus reduces to store those WTMM maxima (WTMMM) only (black dots in Fig. 2B–D). They indicate locally the direction where the signal has the sharpest intensity variation (arrows in Fig. 2B–D). The quantitative characterization of anisotropy is obtained by considering, at every scale *a* > 0, the probability density functions (pdf), $P_a(\mathbf{A})$ of the angles **A** associated with these WTMMM vectors. These pdfs provide the statistical information on any potential directional preference. Using this approach a flat $P_a(\mathbf{A})$ distribution indicates

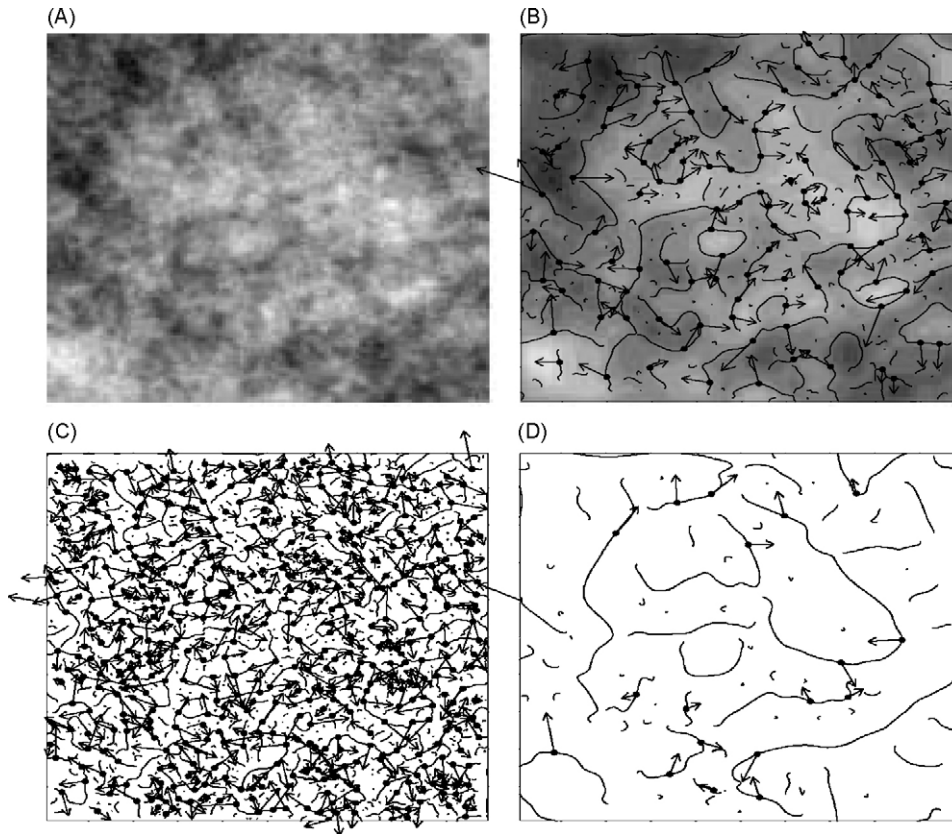


Fig. 2. 2D Wavelet Transform analysis of 2D isotropic fBm simulated surfaces. (A) 32-bit grey-scale coding of the original image. In (B) $a = 2^{2.9}\sigma_W$, (C) $a = 2^{1.9}\sigma_W$ (D) $a = 2^{3.9}\sigma_W$ (where $\sigma_W = 7$ pixels), are shown the maxima chains; the local maxima of M_ψ along these chains are indicated by (●) from which originate an arrow whose length is proportional to M_ψ and its direction (with respect to the x -axis) is given by A_ψ .

locally unprivileged (random) directions of sharpest intensity variation (i.e., isotropy), while any departure from a flat distribution is interpreted as the signature of anisotropy. The $P_a(\mathbf{A})$ distributions were calculated for all individual image segments, and averaged for each data set.

2.6. The 2D Fourier Transform analysis

The (discrete) Fourier Transform samples the underlying periodic structures at regular intervals (here defined by the image pixels). For any 2D image of size $N \times N$ pixels, if $f(x, y)$ represents a grey level at position (x, y) , the Fourier Transform, $F(k_x, k_y)$ of $f(x, y)$ is calculated according to the following equation:

$$F(k_x, k_y) = \sum_{y=0}^{N-1} \sum_{x=0}^{N-1} f(x, y) e^{-i(2\pi/N)(k_x x + k_y y)}, \quad (7)$$

where $k_x = 0, 1, \dots, N-1$ and $k_y = 0, 1, \dots, N-1$. The Fourier Transform $F(k_x, k_y)$ is readily converted into a 2D power spectrum, $P(k_x, k_y)$ by applying the following equation:

$$P(k_x, k_y) = \frac{|F(k_x, k_y)|^2}{N^2}, \quad (8)$$

yielding the weighted distribution of frequencies relative to the Cartesian coordinate. Much like the Wavelet Transform (Eqs. (3)–(5)), the 2D power spectra obtained using the 2D-FT described above, can be further decomposed into angular distribution functions, $P_a(\mathbf{A})$, the coefficients of which directly indicate a directional preference in the original image. This is accomplished by converting the 2D power spectrum into polar coordinates in an analogous way as for the WTMM method (see Eq. (5)).

2.7. Synthetic surfaces

Generating several realizations of simulated 2D fractional Brownian motion (fBm) surfaces is very useful for calibrating image analysis tools and serves as a model of random isotropic rough surfaces [10,11,13]. Since isotropy is rather idealistic in the case of real textures, anisotropic rough surfaces such as fractional Brownian sheets (fBs) are also used for calibration purposes [13]. These surfaces are generated in a similar manner to fBm surfaces, except that the roughness of the former can carry a directional preference (anisotropy). This means that the intensity variation will depend on the direction of interest. Thirty-two (1024×1024) isotropic fBm surfaces and 32 (1024×1024) anisotropic fBs surfaces were generated following standard methods [10,11,13]. These images were analyzed by both the WTMM and Fourier methods, where only the central (512×512) parts were kept for analysis to avoid edge-effects. The resulting probability distributions $P_a(\mathbf{A})$ were used comparatively to assess the departure from isotropy in the experimental image data, and the extent to which the analytical techniques are sensitive to surface anisotropy.

2.8. Anisotropy factor

In order to obtain quantitative information from the pdfs $P_a(\mathbf{A})$, a metric was defined in order to compare them to a unique cosine distribution. We introduce the *anisotropy factor*, F_a , defined for each scale parameter a , as the area between the observed pdfs and the cosine function (see Fig. 6A and B):

$$F_a = \int_{-\pi}^{\pi} |P_a(\mathbf{A}) - \frac{1}{2\pi}(\cos(2\mathbf{A}) - 1)| d\mathbf{A}, \quad (9)$$

where F_a has been normalized in such a way that a theoretically isotropic surface will have a value of $F_a = 1$, while any value less than 1 quantifies a departure from isotropy. Note that this definition of F_a is not perfect and is based specifically on the analysis of the histological images presented in this paper. It provides objective and quantitative information on the strength of anisotropic signature, but there is no indication that a random theoretical anisotropic surface should have the cosine curve signature. One principal advantage of using Eq. (9) is that it takes into account the position of possible features present in the pdfs of $P_a(\mathbf{A})$. Indeed, a surface for which $P_a(\mathbf{A})$ shows peaks at $\pm\pi/2$ will have value of F_a greater than 1. Therefore, this definition of F_a ensures that surfaces showing such anisotropic features that are as strong, but at different angles than 0 and $\pm\pi$ will have corresponding specific values of F_a .

3. Results

3.1. Synthetic surfaces

Before launching the FT and WTMM analyses on the histology images of soft-tissue in-growth into artificial bone implants, two sets of 32 (1024×1024) images were generated, *i.e.*, isotropic and anisotropic synthetic surfaces, in order to calibrate both methods. Averaging the results over 32 (1024×1024) images is sufficient to obtain highly accurate results, as methodically demonstrated in previous publications [10,11,13]. We have first wavelet transformed the fBm (isotropic) and fBs (anisotropic) images with the analyzing wavelets given by Eq. (2), as shown in Figs. 2 and 3, respectively. The maxima chains corresponding to the black edge detection lines in Fig. 2 show random positioning for the simulated isotropic images (fBm) whereas those of the anisotropic images (fBs) shown in Fig. 3 demonstrate a clear vertical tendency. This

vertical behavior becomes more and more pronounced when going to smaller scales (*i.e.*, smaller values of a) and the corresponding arrows converge towards a general alignment to the x -direction. In Fig. 4, are reported the results of the computation of the pdfs $P_a(\mathbf{A})$, *i.e.*, the histograms of the angles of the arrows shown in Figs. 2 and 3, from the set of 32 (1024×1024) images of the simulated isotropic (A and B) and anisotropic (C and D) rough surfaces. In each case the pdfs are shown for four different values of the scale parameter a . As expected, the pdfs of the angles $P_a(\mathbf{A})$ presented in Fig. 4A show a flat distribution, indicating that there are no preferential directions of intensity variations in the *isotropic* fBm surfaces. In contrast, the anisotropic (fBs) images exhibit a pdf that becomes more and more sharply peaked at two values $\mathbf{A} = 0$ and $\pm\pi$, in the limit that the scale parameter is reduced (*i.e.*, when a approaches 0, Fig. 4C). For comparison we have applied the 2D-FT method to the same 32 fBm and fBs surfaces. Consistent with the results obtained with the WTMM method, the 2D-FT calculated pdfs $P_a(\mathbf{A})$ for the *isotropic* fBm surfaces show a flat distribution (Fig. 4B) indicating no directional preferences in their intensity variations. The pdfs associated to the *anisotropic* fBs surfaces become more sharply peaked at two values $\mathbf{A} = 0$ and $\pm\pi$ (Fig. 4D), as the scale parameter goes to zero. It should be noted here that while both techniques demonstrate similar behavior in the pdfs, the width of the pdf $P_a(\mathbf{A})$ features visible in Fig. 4 do vary between the two methods.

3.2. Histological images

Following removal of sub-images that either contained implant sections or that were scratched during sample preparation, a total of 2999 images of (512×512) pixels were analyzed in this study. The results were compiled into 9 categories, depending on the pore size (small, medium, and large—see Section 2) and post-operative time

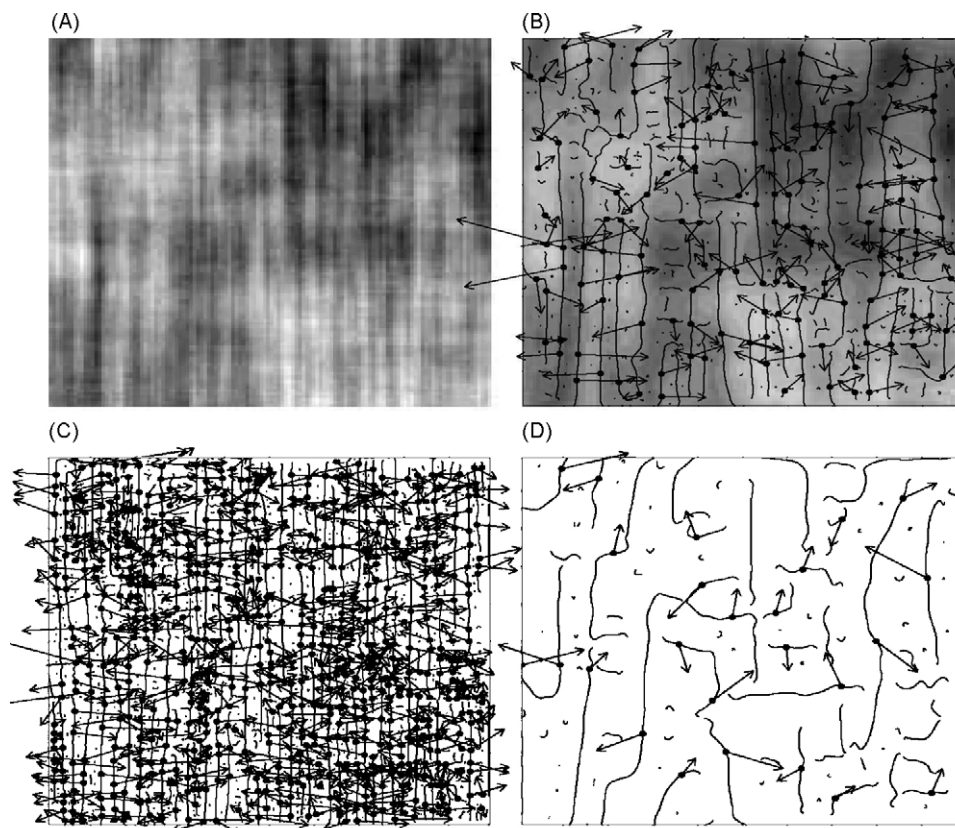


Fig. 3. Same analysis as presented in Fig. 2, but on 2D anisotropic fBs simulated surfaces.

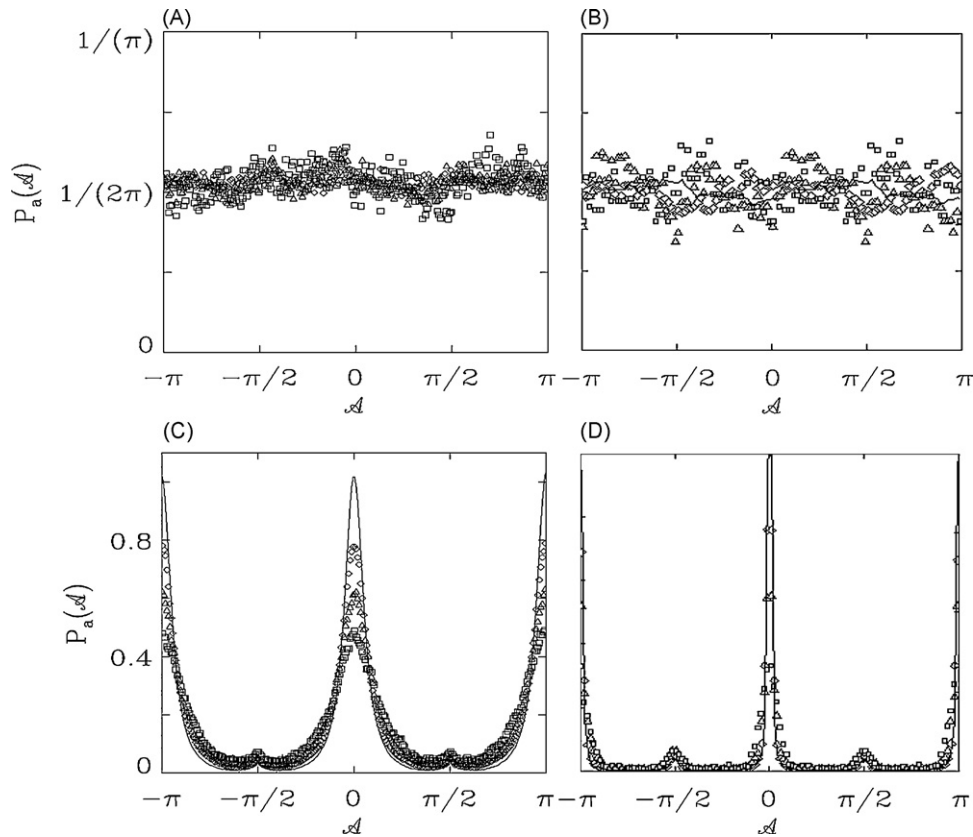


Fig. 4. Pdfs as computed at different scales $a = 1$ (full line), 2 (\diamond), 4 (\triangle), 8 (\square) (in $\sigma_W = 7$ pixel units). The pdfs of the WTMM coefficients ($P_a(\mathcal{A})$ vs. \mathcal{A}) are shown for (A) fBm isotropic surfaces, and (C) fBs anisotropic surfaces. Pdfs of the angularly resolved FT coefficients ($P_a(\mathcal{A})$ vs. \mathcal{A}) are shown for (B) fBm isotropic surfaces, and (D) fBs anisotropic surfaces. Results obtained by averaging over 32 (1024×1024) images.

points (4, 8, and 16 weeks). The anisotropy analysis was performed on all images using both techniques. We have wavelet transformed all histology images and performed the same kind of WTMM analysis as described above. From a visual inspection of Fig. 5, one cannot determine whether the maxima chains show a vertical, horizontal, or any preferential angular tendency. In Fig. 6A and C are reported the results of the computation of only the pdfs $P_a(\mathcal{A})$ for the large pore size, 4-week and 16-week groups respectively for four different values of the scale parameter a . The departure from a flat distribution is a clear sign of anisotropic signature. However, unlike the simulated anisotropic 2D fBs surface presented in Fig. 4, the anisotropy of the soft-tissue images is not scale-dependent. For the soft-tissue, the strength of the anisotropic signature is independent of the size scale considered. For the four different scales presented in Fig. 6A and C, there is no sign of change in shape for the pdfs. This is in strong contrast to Fig. 4C, where there is clearly a change of anisotropic signature with scale.

Since the 2D Fourier analysis is only applicable to images having a homogeneous roughness (i.e., mono-fractal), we followed the standard wavelet-based multifractal analysis procedures [10–13] and determined that all histological images had a mono-fractal signature (data not shown). We have then applied the 2D-FT method to all histology images and obtained the same kind of angular pdf $P_a(\mathcal{A})$ as from the WTMM analysis. In Fig. 6B and D are reported the results of the computation of the pdf $P_a(\mathcal{A})$ using the 2D-FT method, for the large pore size, 4-week and 16-week groups respectively for four different values of the scale parameter a . Again, the departure from a flat distribution is a clear sign of anisotropic signature. Consistent with the results obtained with the WTMM method, the anisotropy of the soft-tissue images is not scale-dependent.

3.3. Calculation of the anisotropy factor

Since the observed anisotropy in the soft-tissue histology samples does not change with scale (scale-independent), the anisotropy factors F_a (see Section 2, Eq. (9)) have been averaged for all scales a considered. Note that for isotropic structures, the anisotropy factor has been theoretically defined to be equal to 1 and therefore any departure of F_a below 1 will quantify the strength of the anisotropic signature: the smaller the value of F_a , the stronger the anisotropic signature. Although only four different scales were presented in Figs. 4 and 6, a total of ten different scales were used for the analysis. These scales can be expressed in units of pixels as $2^a \sigma_W$, where $\sigma_W = 7$ pixels. Note that seven is the minimum number of pixels for the wavelet to be sufficiently resolved [10,11,13,17,18]. The scale parameter a goes from $a = 0$ to $a = 4.5$ with increments of 0.5. This means that the smallest and largest scales considered are $2^a \sigma_W = 7$ pixels and $2^a \sigma_W = 158$ pixels, respectively. Given a pixel size of $0.21 \mu\text{m}$, this translates to physical sizes of ~ 1 to $\sim 33 \mu\text{m}$. The averaged anisotropy factors obtained by the WTMM method and corroborated by the Fourier analysis are listed in Table 1. Also listed in Table 1 are the anisotropy factors calculated by both methods for the isotropic fBm synthetic surfaces, showing a value close to the theoretically expected value of 1. A statistical analysis of the results presented in Table 1 shows that regardless of the pore sizes, the anisotropic signature is strongest at 4 weeks, and then diminishes at 8 weeks, and then diminishes even more and starts to approach isotropy at 16 weeks. A quantitative (t -test) comparison shows that the differences between 4 and 8 weeks, 8 and 16 weeks, as well as 4 and 16 weeks are all highly significant ($>99.99\%$). For the small and medium pore sizes, Fourier analysis results show a strong decrease in anisotropy between weeks 4 and 8 and thereafter in contrast to

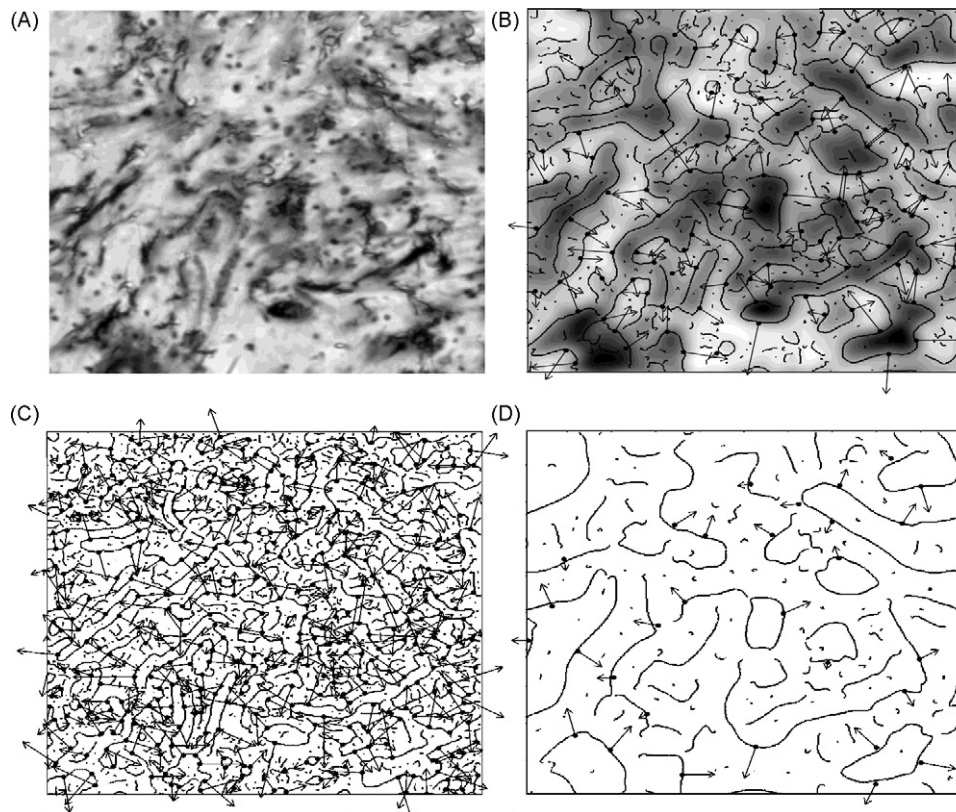


Fig. 5. 2D Wavelet Transform analysis of a sample (512 × 512) sub-image taken from the large pore group, 16-week data. (A) 32-bit grey-scale coding of the original image. In (B) $a = 2^{2.9}\sigma_w$, (C) $a = 2^{1.9}\sigma_w$ (D) $a = 2^{3.9}\sigma_w$ (where $\sigma_w = 7$ pixels), are shown the maxima chains; the local maxima of M_ψ along these chains are indicated by (●) from which originate an arrow whose length is proportional to M_ψ and its direction (with respect to the x-axis) is given by A_ψ .

Table 1

Evolution of the WTMM and FT calculated mean anisotropy factors F_a (Eq. (9)) as a function of pore size and time. For comparison the average F_a values for the isotropic fBm simulated surfaces are shown on the bottom row. From the definition of F_a , pure isotropy corresponds to a value of 1, and any value of F_a below 1 quantifies the anisotropy. Calculations of the anisotropy factors cover a range of scales from ~1 to ~33 μm.

Sample description		Number of (512 × 512) images	Anisotropy factor			
Pore size	Time (weeks)		WTMM		FT	
			Mean	Std Dev	Mean	Std Dev
Small	4	286	0.753	0.017	0.767	0.015
Small	8	364	0.886	0.044	0.918	0.033
Small	16	187	0.887	0.027	0.879	0.027
Medium	4	341	0.701	0.016	0.750	0.012
Medium	8	477	0.876	0.024	0.900	0.022
Medium	16	430	0.904	0.014	0.875	0.021
Large	4	231	0.762	0.020	0.771	0.017
Large	8	368	0.827	0.016	0.852	0.021
Large	16	315	0.925	0.019	0.915	0.016
Isotropic fBm	–	32 (1024 × 1024)	0.987	0.013	0.969	0.019

WTMM, a slight loss of isotropy. Although there is a difference in the mean results, given the magnitude of the standard deviation, this difference is not likely to be significant. The statistical analysis further shows that no correlation exists between the anisotropic strength and pore size. In order to further investigate these results, correlations between anisotropy and pore size were sought, but within each individual animal in order to eliminate the probability of having one animal having reacted drastically differently than others. Such further investigation yielded similar results (data not shown).

4. Discussion

The characterization of soft-tissue in-growth into porous metal implants relies primarily on mechanical testing and secondarily on

qualitative histological analyses [2,3]. We set out to characterize the structure of soft-tissue in-growth into alumina ceramic implants of different pore sizes and at different post-operative time points by objective and rigorous mathematical analysis of histological images. Recognizing the limitations of the Fourier power spectrum approach in terms of its inability to characterize heterogeneity in rough surfaces [10–13], the 2D Wavelet Transform Modulus Maxima method was adapted and used. The Fourier analysis method was used as a complementary approach to add robustness to the results and to ensure that the findings are method independent. The consistency of both methods was first verified by calibration on isotropic and anisotropic synthetic surfaces. It is important to note that the synthetic anisotropic surfaces should not be directly compared to the actual soft-tissue images. Indeed, standard structural anisotropy like the one found in the fractional Brownian sheet (fBs)

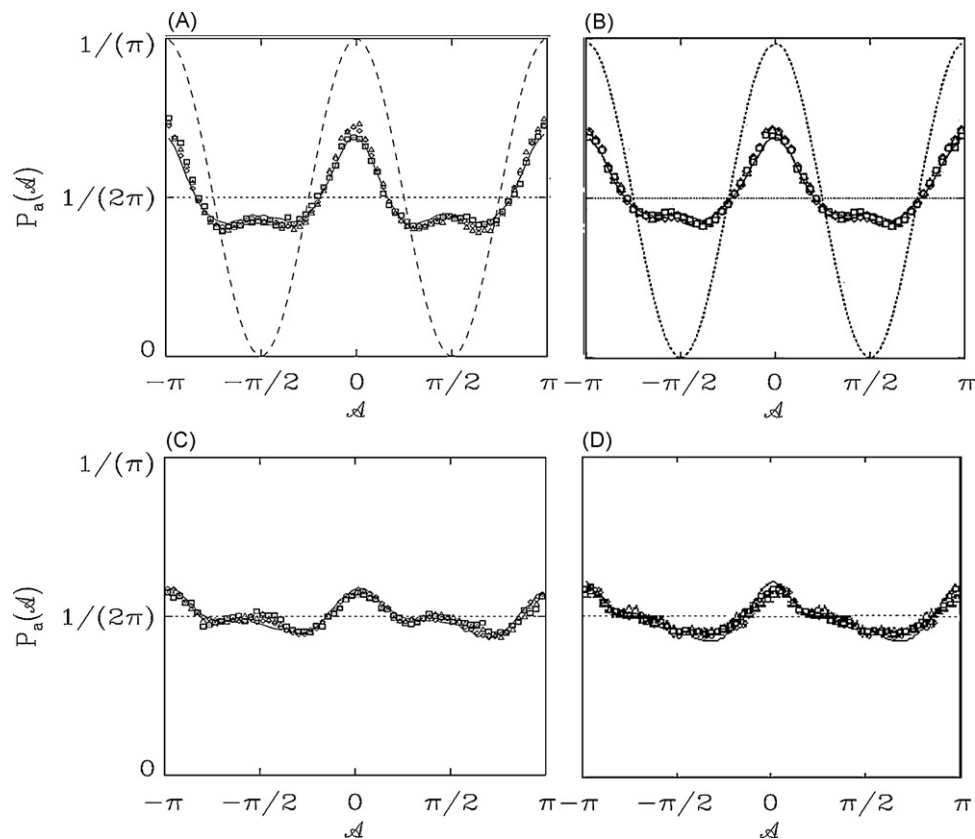


Fig. 6. Pdfs of the WTMM coefficients as computed at different scales $a=1$ (full line), 2 (\diamond), 4 (Δ), 8 (\square) (in $\sigma_w=7$ pixel units) with the first-order analyzing wavelets described by Eq. (2). $P_a(\mathbf{A})$ vs. \mathbf{A} for large pore 4-week group (A), and large pore 16-week group (C). Pdfs of the 2D-FT coefficients as computed at the same four scales. $P_a(\mathbf{A})$ vs. \mathbf{A} for large pore 4-week group (B), and large pore 16-week group (D). These results correspond to averaging over 231 and 315 (512×512) images, respectively. Dotted curves shown in (A) and (B) correspond to the cosine function used in Eq. (9) from which the anisotropy factor is calculated.

models presented here are scale-dependent in that the strength of the anisotropy increases with decreasing spatial scale. Moreover, a quick visual inspection clearly indicates that the fBs structure does not resemble that of the histology images. However, they proved to be perfectly adequate for calibration purposes. For all results presented in this paper, both the WTMM and Fourier analysis yield very similar results, which is a strong validation that the robust quantitative information reported here is indeed valid. Both methods exhibit sensitivity for anisotropy in both the simulated images and the histological images.

One important factor for this study was the quality of the images used for the analysis. The samples were fixed in formalin, embedded in Technovit and stained with H&E and toluidine blue. We believe that these processing choices had minimal effects on the quality of the images for this study. The image analysis was based on detecting the signature of the extracellular matrix, which is mostly type I collagen. Although commercial formalin is not ideal for the fixation of all samples, it is indeed adequate for fixation of the extracellular matrix in this study. The choice of stain used to visualize the extracellular matrix does affect the strength of the signal received. However, because the samples were embedded in Technovit, the choice of stains was limited. The lab has routinely used toluidine blue and H&E for the staining of extracellular matrix components in plastic-embedded samples, and does not believe the choice of stain significantly affected the outcome of this study.

All histological images analyzed in this study exhibited an anisotropic signature, for all size scales considered, *i.e.*, from ~ 1 to $\sim 33 \mu\text{m}$. The images analyzed, however, do not seem to have different anisotropic signatures as a function of pore size, indicating that the pore size may or may not have an influence on the structural growth characteristics of the soft-tissue. Such a structural differ-

ence associated to the artificial implant pore size, if it exists, is not correlated with the strength of the anisotropic signature characterized from the histology images. However, both techniques do show that from the calculated anisotropy factor, there are clear and robust signs of a structural evolution as a function of time. The anisotropy is very strong at 4 weeks (low values of the anisotropy factor), but weakens substantially after 8 and 16 weeks (values closer to 1, isotropy). Our hypothesis is that after only 4 weeks, the soft-tissue has essentially grown directly (vertically) into the artificial implant, *i.e.*, from the exterior towards the center of the implant, which would be responsible for the strong anisotropic signature. After 8 weeks, and even more so after 16 weeks, the tissue is likely to have developed a random tree-like structure and has begun growing and strengthening in all directions (weaker anisotropic signature). This is consistent with previous findings regarding tissue in-growth into porous implants. As implantation time progresses, the density and organization of the tissue inside the pores increases [2], with collagen deposition increasing as the tissue matures [22]. As such, at early time points the main tissue growth activity is concentrated on populating the artificial implant (growing towards the center) while at later time points the tissue is strengthening its structure by filling in the remaining volume, growing in random directions.

The implant material is a hollow porous structure that is placed on “top” of the subcutaneous tissue layer. At the time of wound closure, the pocket was closed and the block was in an initial milieu of blood, and with time over the course of a few days, a serous/plasma rich solution. The initial blood is expected to form to some degree a fibrin clot in and around the lattice of the implant, and the following serous plasma would deliver the pluripotential growth factors that are thought to initiate the in-growth process. The immunohistochemistry of these blocks demonstrated that the pores from

4 weeks onwards are filled with extensive tissue that is Type I collagen. The precise time frame prior to 4 weeks when this occurs is unknown but we have initiated further experimental models in attempt to determine how early this collagen deposition occurs and to define the specific growth factors that demonstrate increased expression to hopefully define the factors that are key to this process and look at them more closely.

The eccentricity of the alumina implants before loading was about 1.2–1.4 (ratio of longest pore length to smallest). Because all of the implants were produced using a similar technique and the eccentricity is the same for them all, this should not have an effect on the conclusions made in our study.

4.1. Future work

It will be interesting to determine what is the *ideal* anisotropic structure from analyzing native tissue. Characterizing such an anisotropic signature will be the first step towards better understanding the biophysical mechanisms responsible for soft-tissue in-growth. Once these mechanisms are better understood, structural anisotropic models will be developed and translated to algorithms for generating more realistic anisotropic rough surfaces than the fractional Brownian sheets. It is interesting to note that the scale-independent anisotropic signature found in the histology images presented here is similar to the observed anisotropic signature found in the Galactic inter-spiral-arms formed of hydrogen gas [13,19], which definitely suggests that some unknown fluid dynamics are responsible for producing such a structural signature.

Acknowledgements

Many thanks to Dr. Alain Arneodo for discussions and technical assistance. This work was funded by Stryker Orthopaedics.

Conflict of interest

The authors declare no conflict of interest.

References

- [1] Bobyn JD, Toh KK, Hacking SA, Tanzer M, Krygier JJ. Tissue response to porous tantalum acetabular cups: a canine model. *J Arthroplasty* 1999;14(3): 347–54.
- [2] Hacking SA, Bobyn JD, Toh K, Tanzer M, Krygier JJ. Fibrous tissue ingrowth and attachment to porous tantalum. *J Biomed Mater Res* 2000;52(4):631–8.
- [3] Dickey ID, Hugate RR, Reach JS, Zobitz ME, Zhang R, Dimaano N, et al. Soft tissue in-growth and attachment to alumina ceramic foam: an in-vivo canine study. *Trans Orthop Res Soc* 2005;30:283.
- [4] Gottsauner-Wolf F, Egger EL, Markel MD, Schultz FM, Chao EY. Fixation of canine tendons to metal. *Acta Orthop Scand* 1994;65(2):179–84.
- [5] Gottsauner-Wolf F, Egger EL, Schultz FM, Sim FH, Chao EY. Tendons attached to prostheses by tendon-bone block fixation: an experimental study in dogs. *J Orthop Res* 1994;12(6):814–21.
- [6] Gottsauner-Wolf F, Grabowski JJ, Chao EY, An KN. Effects of freeze/thaw conditioning on the tensile properties and failure mode of bone-muscle-bone units: a biomechanical and histological study in dogs. *J Orthop Res* 1995;13(1):90–5.
- [7] Reach Jr JS, Dickey ID, Zobitz ME, Adams JE, Scully SP, Lewallen DG. Direct tendon attachment and healing to porous tantalum: an experimental animal study. *J Bone Joint Surg Am* 2007;89(5):1000–9.
- [8] Fourier J. The analytical theory of heat. Cambridge, UK: Cambridge University Press; 1822.
- [9] Enomae T, Han YH, Isogai A. Destructive determination of fiber orientation distribution of paper surface by image analysis. *Nordic Pulp Paper Res J* 2006;21(2):253–9.
- [10] Arneodo A, Decoster N, Roux S. A wavelet-based method for multifractal image analysis. I. Methodology and test applications on isotropic and anisotropic random rough surfaces. *Eur J Phys B* 2000;15:567–600.
- [11] Arneodo A, Decoster N, Kestener P, Roux S. A wavelet-based method for multifractal image analysis: from theoretical concepts to experimental applications. In: Hawkes PW, editor. *Advances in imaging and electron physics*. Academic Press; 2003. p. 1.
- [12] Decoster N, Arneodo A, Roux S. A wavelet-based method for multifractal image analysis. II. Applications to synthetic multifractal rough surfaces. *Eur J Phys B* 2000;15:739–64.
- [13] Khalil A, Joncas G, Nekka F, Kestener P, Arneodo A. Morphological analysis of HI features. II. Wavelet-based multifractal formalism. *Astrophys J Suppl Ser* 2006;165:512–50.
- [14] Roux S, Decoster N, Arneodo A. A wavelet-based method for multifractal image analysis. III. Applications to high-resolution satellite images of cloud structure. *Eur J Phys B* 2000;15:765–86.
- [15] Kestener P, Lina JM, St-Jean P, Arneodo A. Wavelet-based multifractal formalism to assist in diagnosis in digitized mammograms. *Image Anal Stereol* 2001;20:169–74.
- [16] Kestener P. Analyse multifractale 2D et 3D a l'aide de la transformation en ondelettes: application en mammographie et en turbulence developpee. In: *Sciences de l'Ingenieur*. Bordeaux: Universite de Bordeaux I; 2003. p. 225.
- [17] Khalil A, Grant JL, Caddle LB, Atzema E, Mills KD, Arneodo A. Chromosome territories have a highly nonspherical morphology and nonrandom positioning. *Chromosome Res* 2007;15(7):899–916.
- [18] Caddle LB, Grant JL, Szatkiewicz J, van Hase J, Shirley BJ, Bewersdorf J, et al. Chromosome neighborhood composition determines translocation outcomes after exposure to high-dose radiation in primary cells. *Chromosome Res* 2007;15(8):1061–73.
- [19] Khalil A. Analyse structurelle de l'hydrogene atomique dans le plan de la Galaxie. In: *Departement de physique*. Quebec: Universite Laval; 2004. p. 218.
- [20] Mallat S, Hwang WL. Singularity detection and processing with wavelets. *IEEE Trans Inform Theory* 1992;38:617.
- [21] Mallat S, Zhong S. Characterization of signals from multiscale edges. *IEEE Trans Pattern Anal Machine Intell* 1992;14:710.
- [22] Bobyn JD, Wilson GJ, MacGregor DC, Pilliar RM, Weatherly GC. Effect of pore size on the peel strength of attachment of fibrous tissue to porous-surfaced implants. *J Biomed Mater Res* 1982;16(5):571–84.